crystals

MDPI

Supplementary Materials

Flexible and Structural Coloured Composite Films from Cellulose Nanocrystals /Hydroxypropyl Cellulose Lyotropic Suspensions

Diogo V. Saraiva, Ricardo Chagas, Beatriz M. de Abreu, Cláudia N. Gouveia, Pedro E. S. Silva, Maria Helena Godinho and Susete N. Fernandes *

i3N/CENIMAT, Department of Materials Science, NOVA School of Science and Technology, NOVA University Lisbon, Campus de Caparica, 2829-516, Caparica, Portugal; dv.saraiva@campus.fct.unl.pt (D.S.); r.chagas@fct.unl.pt (R.C.); b.abreu@campus.fct.unl.pt (B.A.); c.gouveia@campus.fct.unl.pt (C.G.); pes.silva@fct.unl.pt (P.S.); mhg@fct.unl.pt (M.G.)

* Correspondence: sm.fernandes@fct.unl.pt

Received: 3 January 2020; Accepted: 12 February 2020; Published: 16 February 2020

1-AFM Analysis

In order to measure the CNC particles' average length and width, Atomic Force Microscopy (AFM) data was acquired using an Asylum Re-search MFP-3D standalone system in tapping mode, with commercially available silicon AFM probes (scanning frequency of 300 kHz, k = 26 N/m). The analysed CNC particles were prepared by casting 1 µL droplets of an extremely diluted suspension of CNC in water (0.01 wt.%) onto a mica substrate (Muscovite Mica, V-5 from Electronic Microscopy Sciences). Immediately before deposition, the suspension was sonicated for an energy input of 18 Kj g^{-1} suspension.

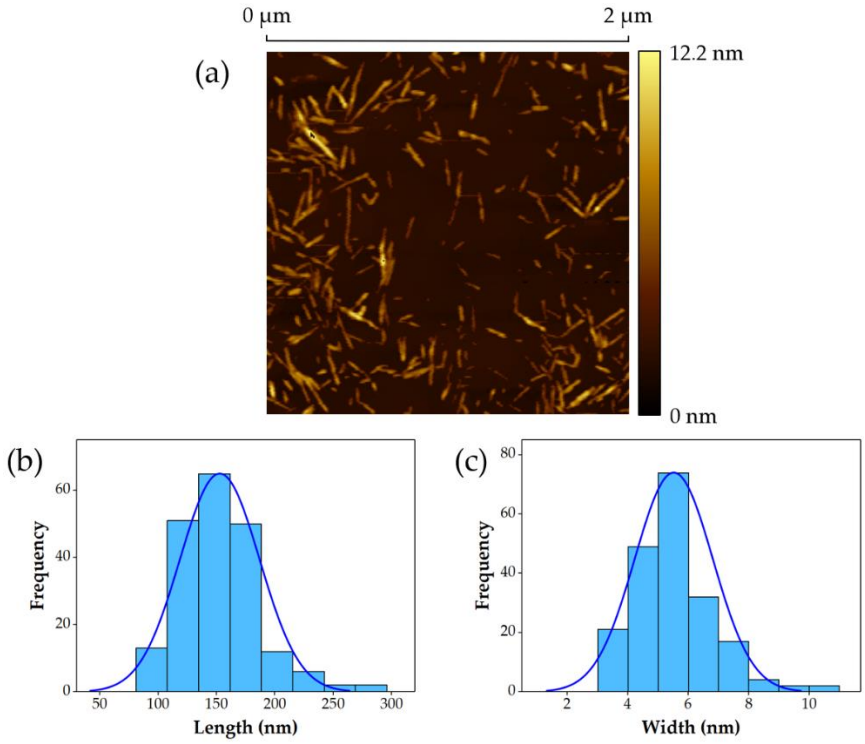

Figure S1. (**a**) Representative portion of an AFM image of dispersed CNC used for particle size distribution; (**b**), (**c**) CNC length and width distribution histograms, respectively, overlaid with normal distribution curves.

From a 10 × 10 μm² square region AFM image, the CNC rods were measured in average length and width. Individual rod measurements were carried out using the freeware Gwyddion (version 2.52, [1]). CNC width values were not obtained from measurements done perpendicularly to each rod, but rather by using a method described by Honorato-Rios et al. [2], where we measured the height profile along each individual rod. For each sample, 200 rods were measured individually and the CNCs' average length and width were calculated to be 153 ± 34 nm and 6 ± 2 nm, respectively. This particular CNC sample's aspect ratio, obtained simply by dividing the average length by the average width, is approximately 26.

2-Bend Test Schematic Representation

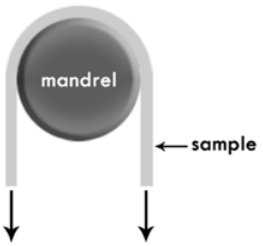

Figure S2. Schematic representation of the bend-test configuration showing a sample bent around a mandrel.

3-LC Behaviour of the Produced CNCs

In order to understand the HPC/CNCs lyotropic phase, first, the liquid crystalline behaviour of the produced CNCs, while suspended in water, was assessed. To do so, aqueous colloidal suspensions with different concentrations of CNCs, ranging from 1.5 to 8.5 wt.% were prepared and allowed to settle in a sealed container. The first vial in Figure 1a (manuscript) with a CNCs suspension with a concentration of 3.3 wt.% shows, as an example, the phase separation behaviour of the CNCs in water, where it was possible to see the appearance of birefringence induced by the presence of the chiral nematic mesophase, observed at the bottom of the vial. In our systems, this coexistence of anisotropic phase occurs at a CNCs concentration higher than 2.2 wt.% and below 2.6 wt.%, as can be seen by the plot of the volume of the anisotropic fraction as a function of CNCs concentration **Error! Reference source not found.**a. Although the anisotropic volume fraction increases with the content of CNCs in the colloidal suspension this increment is not completely linear. If one considers the Onsager model, this variation should be linear [3]. However it has to be noted that, since we have electronegative charged nanoparticles, as its concentration increases in the colloidal suspension, the ionic strength of the suspension is altered [2]. Indeed, Dong et al. have shown that if the ionic strength of the suspensions is kept constant, by adding a salt, as the concentration of CNCs rises a linear dependence will be obtained [4]. Although a somewhat lower value for critical concentration is observed for our sample, when compared with several samples described in the literature, where values higher than 4.5 wt.% of CNCs are reported necessary to promote phase separation, the exact comparison is not always possible since acid-hydrolysis conditions are normally omitted. If one considered that our CNCs were obtained from an acid hydrolysis process with the acid solution to cellulose ratio of 8.5:1, a 45 °C reaction temperature, 45 min. Reaction time, which generates particles with average dimensions of 153 ± 34 nm × 6 ± 2 nm (length × width) and a surface charge of 0.72%S, our values are in line with what is observed by Abitol et al. [5]. These authors demonstrate that never-dried CNCs, from similar acid-hydrolysis conditions, with particle sizes of 100 ± 10 nm × 5.5 ± 0.5 nm (length × width) and surface charges of 0.58%S and 0.89%S, present an onset of phase separation for CNCs content values of 2.5 and 5.1 wt.%, respectively. If one looks at these values, our critical concentration to promote phase separation is still low, but considering the recent work published by Honorato-Rios et al., where the authors demonstrate that longer rods present a lower onset of phase transition, our value can be justified [2]. If the suspensions are placed in a rectangular sealed vial, the observation with crossed-polars by optical microscopy allows us to see the typical textures of CNCs

LC suspensions, **Error! Reference source not found.**b–d. In these images, insets of the square red region were introduced in order to help the discussion of the results. In **Error! Reference source not found.**b, corresponding to the colloidal suspension with 2.6 wt.% of CNCs, the typical tactoids, described as ellipsoid order regions with birefringent parallel fingerprints, are surrounded by an isotropic suspension. In these segments, the distance between two consecutive dark fringes is around 7 μm, corresponding to half the value of the chiral nematic pitch, being the optical axis of the helicoidal arrangement is parallel to the surface of the vial. As the concentration of the CNCs in suspension increases, the tactoids tend to coalesce, settle and the fingerprint-like texture evolves, as can be seen in **Error! Reference source not found.**c for a 4.5 wt.% suspension of CNCs [6,7]. The decrease of the pitch value as the concentration of nanoparticles in suspension increases is noticeable, since the distance between fringes is reduced. For a higher concentration only with a higher magnification it is possible to visualise the fingerprint texture, as can be seen in **Error! Reference source not found.**d [8].

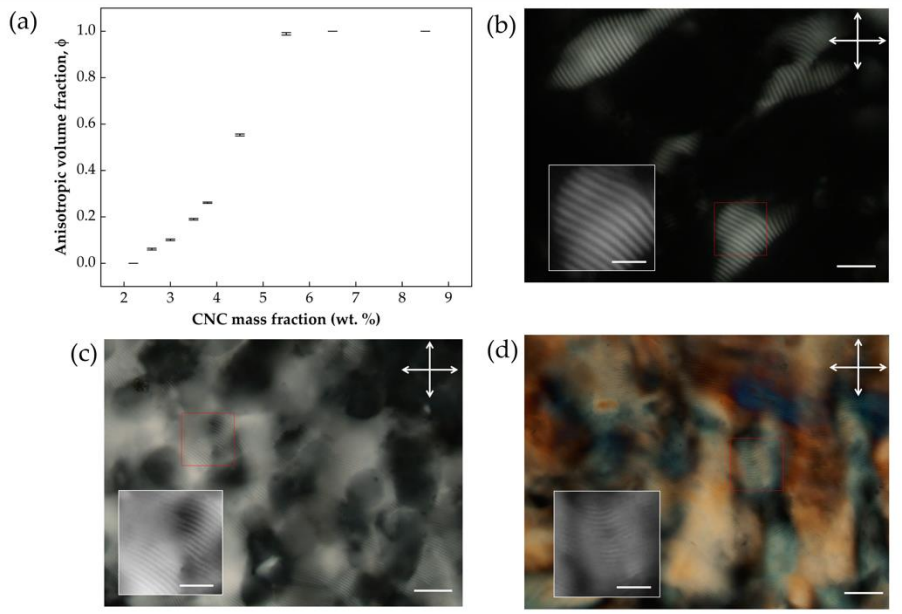

Figure S3. (**a**) Phase diagram of the CNCs/H_2O system represented by the volume fraction ϕ of the anisotropic to isotropic phase as a function of the concentration of CNCs in the colloidal suspensions; (**b–d**) Crossed-polarised optical microscope images obtained at the bottom of the hollow glass tube in transmission mode of CNCs suspension with a CNC concentration of 2.6, 4.5, and 8.5 wt.%, respectively (insets of the red square regions showing the banded fingerprint in a small area). Scale bars: (b–d) 50 μm; inset (b–d) 25 μm.

4-FTIR Analysis of MCC, CNC, HPC and CNC/HPC Composite Films

Chemical characterisation via Fourier Transform Infrared (FTIR) spectroscopy was performed on samples of MCC and CNC. FTIR spectra were obtained using an attenuated total reflectance (ATR) sampling accessory (Smart iTR) equipped with a single-bounce diamond crystal on a Thermo Nicolet 6700 spectrometer. Spectra were acquired at room temperature, with data ranging from 4000 to 400 cm^{-1}, with a 0.5 cm^{-1} resolution. Scans were made with an incident angle of 45°.

In both spectra, several cellulose-characteristic absorption bands are present. The wide absorption band, centred at 3320 cm^{-1}, is associated with stretching O-H bonds, indicative of hydrogen bonds in both samples. The absorption band located at 890 cm^{-1} is linked with stretching C-O-C bonds, present in β-1,4 linkages. Though both spectra have several other identified cellulose-characteristic absorption bands, only the CNC sample's spectrum includes, at around 820 cm^{-1}, an absorption band assigned to stretching S-O bonds, confirming the presence of sulphate groups on the sample, due to it having undergone an acid hydrolysis [9,10].

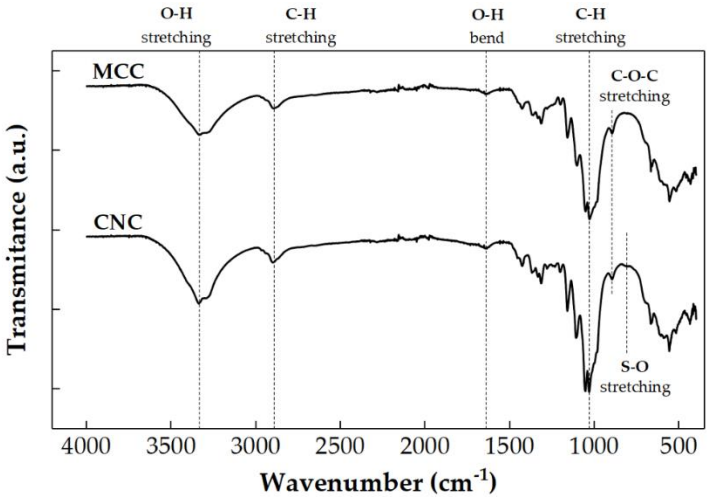

Figure S4. FTIR spectra of microcrystalline cellulose (MCC-Avicel® PH-101) and cellulose nanocrystals (CNC). The vertical dashed lines mark various cellulose-characteristic absorption bands.

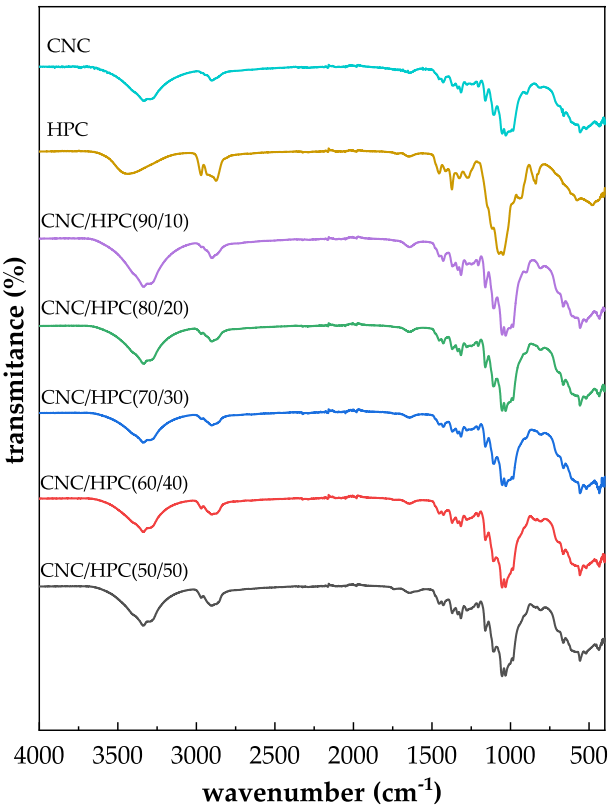

Figure S5. FTIR spectra of CNC, HPC and CNC/HPC composite films in different ratios.

5-XRD Analysis

The diffractograms obtained for MCC and CNC samples are presented below, in **Error! Reference source not found.**.

Crystallinity index (Ic) was calculated for each sample using the empirical method presented by Segal et al. [11], using select diffraction peaks identified in **Error! Reference source not found.**.

In table S1 a list of diffraction peaks, and their locations, are displayed along with the respective Ic value calculated for each sample.

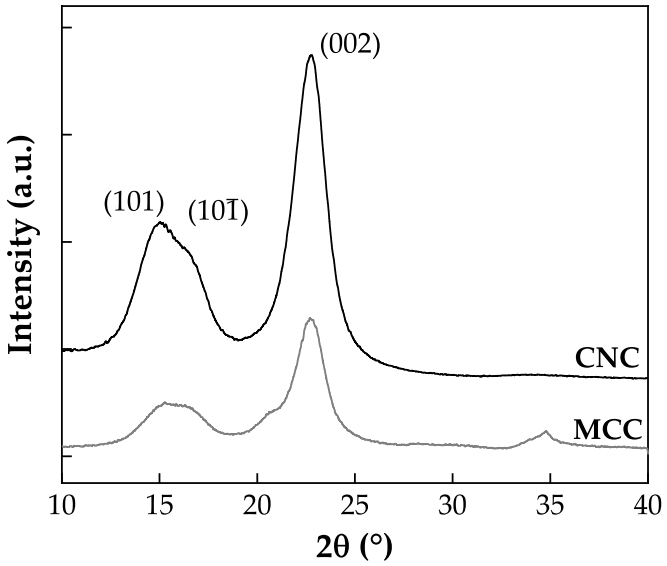

Figure S6. X-ray diffraction spectra for MCC and CNC samples, with labelled crystalline peaks.

Table S1. Crystalline peak locations for the MCC and CNC samples' XRD spectra, along with their respective calculated crystallinity index.

Sample	cr(101)	cr(10$\bar{1}$)	cr(002)	Crystallinity index (I_C)
MCC	15.2°	16.4°	22.7°	75.7%
CNCs	14.9°	16.3°	22.7°	87.8%

The locations of the marked crystalline peaks are in good accordance with [12], as is the increase in crystallinity index from the MCC sample to the CNCs sample [13].

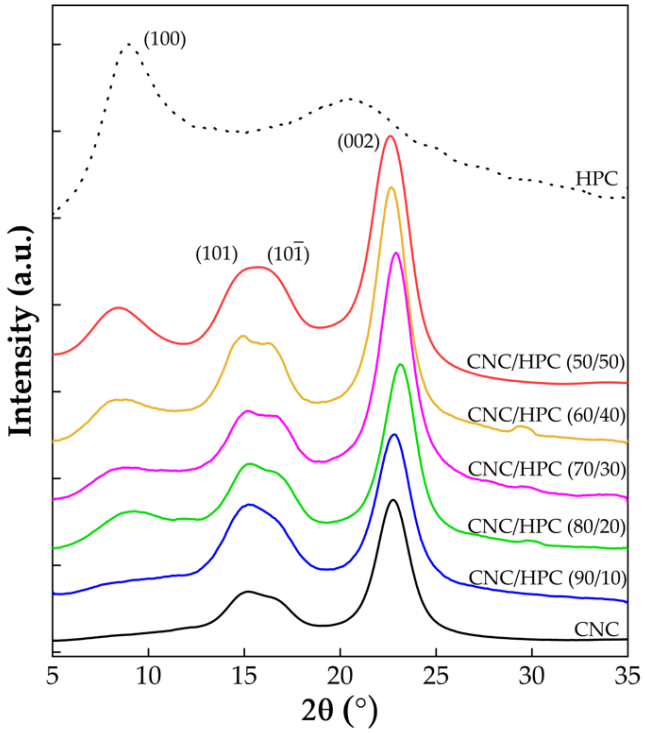

Figure S7. X-ray diffraction spectra for CNC, HPC and CNC/HPC composites, with labelled crystalline peaks.

6- Calculated and Measured pitch Values in CNC/HPC Composite Films

Table S2. Various measured values from CNC and CNC/HPC composite films.

Composite Sample		CNC	CNC/HPC (90/10)	CNC/HPC (80/20)	CNC/HPC (70/30)	CNC/HPC (60/40)	CNC/HPC (50/50)
UV-VIS-NIR spectra	λ_{max} (nm)	506	570	900	1035	1135	1235
	P predicted (nm)	324	370	596	695	772	852
Cross-section SEM	P/2 (nm)	157 ± 29	191 ± 29	294 ± 24	340 ± 34	368 ± 42	419 ± 94
	P predicted (nm)	314	382	588	680	736	838
	λ_{max} predicted (nm)	490	588	888	1013	1082	1215
Refractive index[1] (*n*)		1.56	1.54	1.51	1.49	1.47	1.45
Film thickness (μm)		26 ± 10	31 ± 16	30 ± 12	37 ± 16	38 ± 18	35 ± 8

[1]Values estimated with the weighted percentage of each cellulosic component in the composite mixture

7-Fingerprint Texture Observed at the Microscale in the CNC and CNC/HPC Composite Films

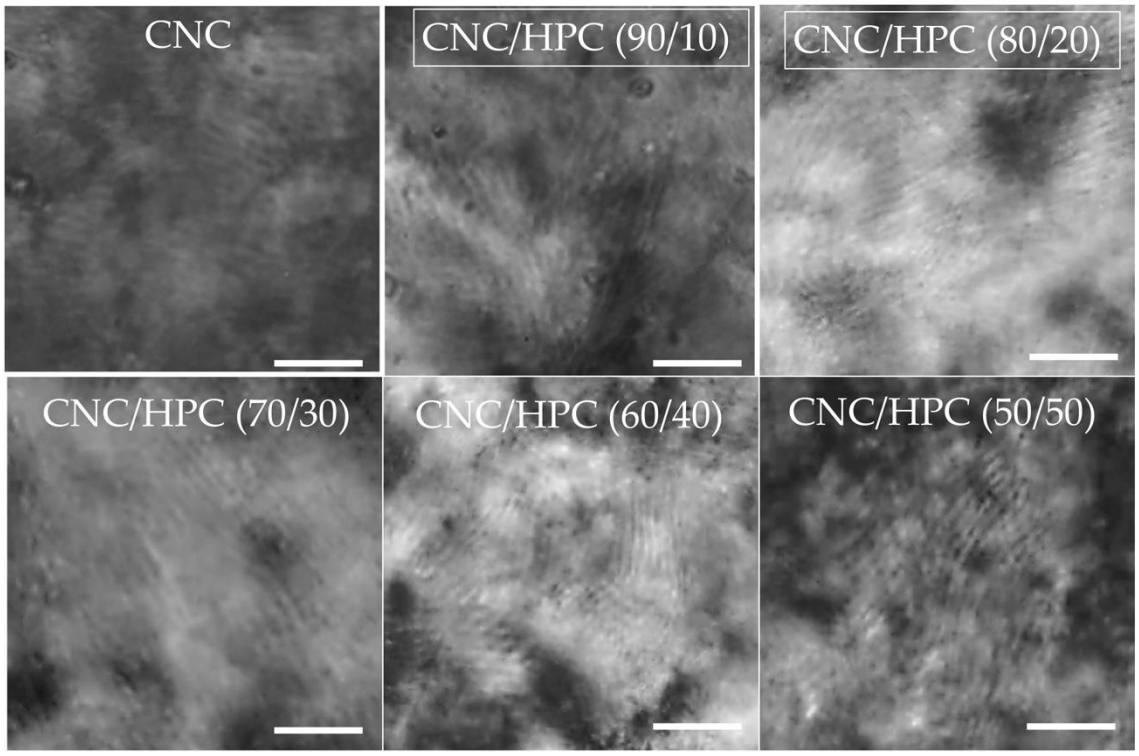

Figure S8. POM images in greyscale obtained with crossed-polars and in transmission mode of the central regions of neat CNCs and CNCs/HPC films, where fingerprint textures are most visible. Scale bars: 25 μm.

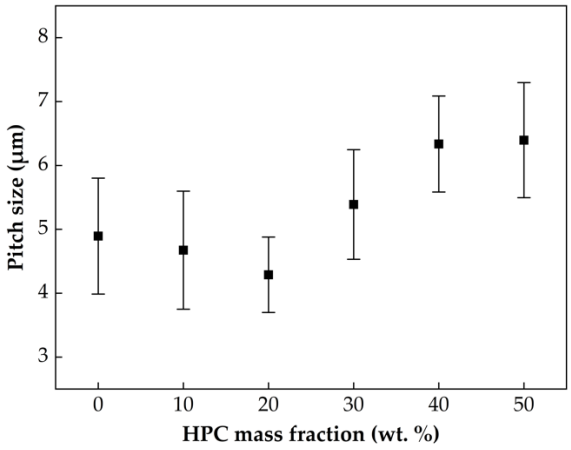

Figure S9. Estimated pitch values measured at the surface of the films CNC and CNC/HPC as a function of HPC composition in the composite system.

8-TGA/DSC Analysis

A thermogravimetric analysis (TGA) was performed using a Netzsch 449 F3 Jupiter® simultaneous thermal analyser. Each sample was heated from 25 to 550 °C, at a heating rate of 10 °C/min.

The TG curve for the MCC sample shows a small decrease in relative mass below 100 °C, due to the evaporation of residual water embedded in the sample. The sample's mass shows little to no change as temperature increases up to around 300 °C, where weight rapidly decreases until 370 °C, accompanied by an endothermic spike in the DSC curve, indicating a typical gravimetric event of cellulose pyrolysis [14]; as the analysis reaches its end, sample mass steadily decreases. The CNCs sample displays weight loss up to 120 °C followed by the start of a two-step pyrolysis reaction (whereas its precursor showed a one-step pyrolysis event): a low-temperature process from 140 °C to 230 °C and a high-temperature process from around 300 °C until the end of the analysis. The presence of sulphate groups has a dehydrating effect on the structure, facilitating the extraction of water from within the structure, and leading to the removal of oxygen, thus preventing the main means of mass loss during the pyrolysis process, which is the emission of CO and CO_2. Because of this, we are left with a larger fraction of material, at the end of the test. [15] Similar DSC-TG curves were obtained by Morais et al. [16].

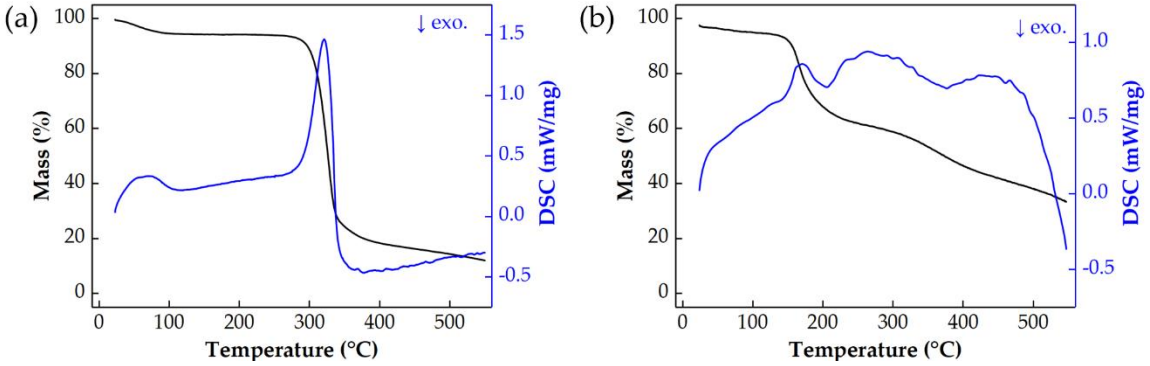

Figure S10. TGA and DSC curves for samples a) MCC and b) CNC.

TGA curves and mass loss rates with respect to temperature were plotted for each sample. From these the moisture content could be determined and included in the following table (table S3) The TgA/DTG curves of two other CNCs' (CNCA1 and CNCA2) sample obtained from the same starting material and experimental conditions, however from different batches were also analysed. It is

important to notice that the set of films were produced at the same relative humidity (60%–70%) and kept at the same relative humidity (40%).

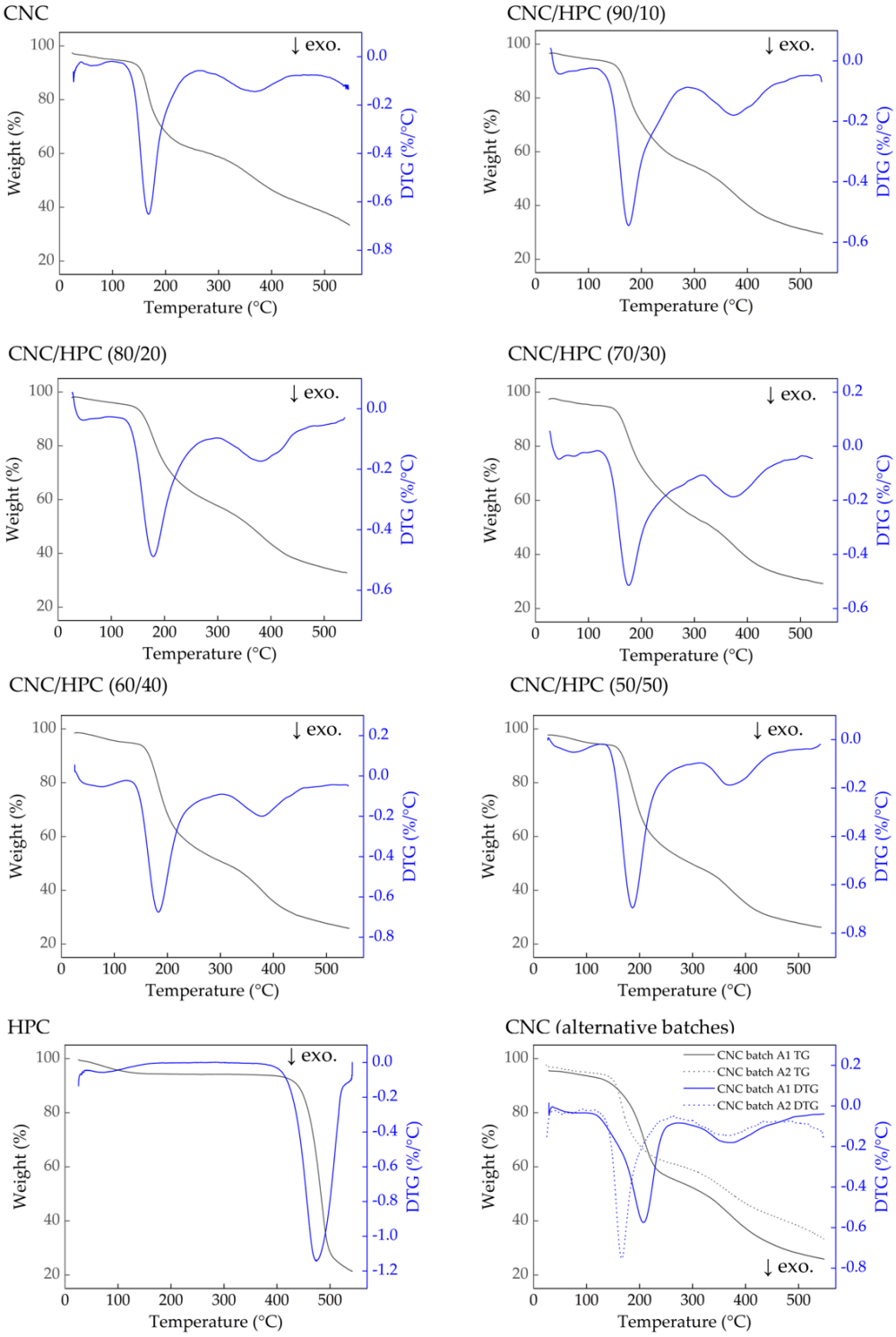

Figure S11. TGA and respective DTG curves for CNC, HPC and CNC/HPC composites. The bottom-right graph displays two separate CNC batches produced under conditions identical to the batch of CNCs.

Table S3. Estimates of the amount of moisture in each CNC, HPC and CNC/HPC composite film analysed by TGA/DTG. These values are measured from the TGA curves in **Error! Reference source not found.**.

Sample	CNC	CNC/ HPC (90/10)	CNC/ HPC (80/20)	CNC/ HPC (70/30)	CNC/ HPC (60/40)	CNC/ HPC (50/50)	CNC A1	CNC A2	HPC
Total water content (%)	2.47	3.54	3.16	2.89	3.99	3.74	2.62	3.47	1.16

Some studies have shown that neat CNCs [17] or even CNCs/PEG [18] films present a shift in the maximum reflected wavelength to higher values when an increase in the relative humidity at which they are exposed occurs. Since hydroxypropyl cellulose is a hygroscopic polymer and can sorb water, one could assume that as the amount of HPC increases in the composite system, the amount of retained moisture in the system would increase. This increment in the hygroscopically sorbed moisture would explain the increase in the maximum reflected wavelength observed. The retained moisture can be determined by TgA analysis since water (free and bound) would be released from the film in the range of temperatures from 25 to 100 °C. From the total water content (**Error! Reference source not found.**), estimated from the TGA/DTG curves (**Error! Reference source not found.**), it was possible to see a slight increase in the moisture content, as the amount of HPC in the composite sample increases. Maximum moisture content of 3.99% was obtained for the sample with 40 wt.% of HPC while 2.47% obtained for pristine CNCs. Furthermore, the results show no linear increase on the water content as the HPC amount in the sample increases, as would be expected if the presence of HPC induces an increase in the amount of the retained moisture. A similar analysis was performed in two other batches of pristine CNCs, obtained with the same experimental conditions and from the same starting material. If one compares the water content values in table S3 for sample CNC and CNCA1, 2.47% versus 3.16, they seemed to indicate that the variation of water content observed for samples with HPC are all within the expected values for CNCs films. Indeed, the values obtained are within the range of adsorbed water existent in CNCs that is usually estimated at around 2 wt.%–5 wt.%, as described by Vanderfleet et al.[19], or by Roman and Witer [20]. From the results obtained in this analysis, the effect of the hygroscopically sorbed moisture in the pitch values is not expected, considering relative humidity of our working conditions.

References

1. Gwyddion website, http://imagej.Nih.Gov/ij/, accessed: 1 May 2018.
2. Honorato-Rios, C.; Lehr, C.; Schütz, C.; Sanctuary, R.; Osipov, M.A.; Baller, J.; Lagerwall, J.P.F. Fractionation of cellulose nanocrystals: Enhancing liquid crystal ordering without promoting gelation. *NPG Asia Materials* **2018**, *10*, 455-465.
3. Honorato-Rios, C.; Kuhnhold, A.; Bruckner, J.R.; Dannert, R.; Schilling, T.; Lagerwall, J.P.F. Equilibrium liquid crystal phase diagrams and detection of kinetic arrest in cellulose nanocrystal suspensions. *Frontiers in Materials* **2016**, *3*, art. 21. [https://doi.org/10.3389/fmats.2016.00021].
4. Dong, X.M.; Kimura, T.; Revol, J.-F.; Gray, D.G. Effects of ionic strength on the isotropic−chiral nematic phase transition of suspensions of cellulose crystallites. *Langmuir* **1996**, *12*, 2076-2082. [https://doi.org/10.1021/la950133b].
5. Abitbol, T.; Kam, D.; Levi-Kalisman, Y.; Gray, D.G.; Shoseyov, O. Surface charge influence on the phase separation and viscosity of cellulose nanocrystals. *Langmuir* **2018**, *34*, 3925-3933. [https://www.ncbi.nlm.nih.gov/pubmed/29513998].
6. Revol, J.F.; Bradford, H.; Giasson, J.; Marchessault, R.H.; Gray, D.G. Helicoidal self-ordering of cellulose microfibrils in aqueous suspension. *Int J Biol Macromol* **1992**, *14*, 170-172. [https://doi.org/10.1016/S0141-8130(05)80008-X].
7. Wang, P.X.; Hamad, W.Y.; MacLachlan, M.J. Structure and transformation of tactoids in cellulose nanocrystal suspensions. *Nat. Commun.* **2016**, *7*, 11515. [http://www.ncbi.nlm.nih.gov/pubmed/27143197].
8. Hu, Z.; Cranston, E.D.; Ng, R.; Pelton, R. Tuning cellulose nanocrystal gelation with polysaccharides and surfactants. *Langmuir* **2014**, *30*, 2684-2692. [https://doi.org/10.1021/la404977t].

9. Abidi, N.; Hequet, E.; Cabrales, L.; Gannaway, J.; Wilkins, T.; Wells, L.W. Evaluating cell wall structure and composition of developing cotton fibers using fourier transform infrared spectroscopy and thermogravimetric analysis. **2008**, *107*, 476-486. [https://onlinelibrary.wiley.com/doi/abs/10.1002/app.27100].
10. Gaspar, D.; Fernandes, S.N.; de Oliveira, A.G.; Fernandes, J.G.; Grey, P.; Pontes, R.V.; Pereira, L.; Martins, R.; Godinho, M.H.; Fortunato, E. Nanocrystalline cellulose applied simultaneously as the gate dielectric and the substrate in flexible field effect transistors. *Nanotechnology* **2014**, *25*, 094008. [http://dx.doi.org/10.1088/0957-4484/25/9/094008].
11. Segal, L.; Creely, J.J.; Martin, A.E.; Conrad, C.M. An empirical method for estimating the degree of crystallinity of native cellulose using the x-ray diffractometer. *Textile Research Journal* **1959**, *29*, 786-794. [https://doi.org/10.1177/004051755902901003].
12. Alves, L.; Medronho, B.; Antunes, F.E.; Fernández-García, M.P.; Ventura, J.; Araújo, J.P.; Romano, A.; Lindman, B. Unusual extraction and characterization of nanocrystalline cellulose from cellulose derivatives. *Journal of Molecular Liquids* **2015**, *210*, 106-112. [http://www.sciencedirect.com/science/article/pii/S0167732214005868].
13. Moon, R.J.; Martini, A.; Nairn, J.; Simonsen, J.; Youngblood, J. Cellulose nanomaterials review: Structure, properties and nanocomposites. *Chem Soc Rev* **2011**, *40*, 3941-3994. [https://www.ncbi.nlm.nih.gov/pubmed/21566801].
14. Bradbury, A.G.W.; Sakai, Y.; Shafizadeh, F. A kinetic model for pyrolysis of cellulose. **1979**, *23*, 3271-3280. [https://onlinelibrary.wiley.com/doi/abs/10.1002/app.1979.070231112].
15. Kim, D.-Y.; Nishiyama, Y.; Wada, M.; Kuga, S.J.C. High-yield carbonization of cellulose by sulfuric acid impregnation. **2001**, *8*, 29-33. [https://doi.org/10.1023/A:1016621103245].
16. Morais, J.P.S.; Rosa, M.d.F.; de Souza Filho, M.d.s.M.; Nascimento, L.D.; do Nascimento, D.M.; Cassales, A.R. Extraction and characterization of nanocellulose structures from raw cotton linter. *Carbohydrate Polymers* **2013**, *91*, 229-235. [http://www.sciencedirect.com/science/article/pii/S0144861712007825].
17. Bumbudsanpharoke, N.; Lee, W.; Chung, U.; Ko, S. Study of humidity-responsive behavior in chiral nematic cellulose nanocrystal films for colorimetric response. *Cellulose* **2018**, *25*, 305-317. [https://doi.org/10.1007/s10570-017-1571-8].
18. Yao, K.; Meng, Q.; Bulone, V.; Zhou, Q. Flexible and responsive chiral nematic cellulose nanocrystal/poly(ethylene glycol) composite films with uniform and tunable structural color. *Adv. Mater.* **2017**, *28*, 1701323. [http://dx.doi.org/10.1002/adma.201701323].
19. Vanderfleet, O.M.; Reid, M.S.; Bras, J.; Heux, L.; Godoy-Vargas, J.; Panga, M.K.R.; Cranston, E.D. Insight into thermal stability of cellulose nanocrystals from new hydrolysis methods with acid blends. *Cellulose* **2019**, *26*, 507-528. [https://doi.org/10.1007/s10570-018-2175-7].
20. Roman, M.; Winter, W.T. Effect of sulfate groups from sulfuric acid hydrolysis on the thermal degradation behavior of bacterial cellulose. *Biomacromolecules* **2004**, *5*, 1671-1677. [https://doi.org/10.1021/bm034519].